1   **Derivation of aerosol fluorescence and water vapor Raman depolarization ratios from lidar**

2   **measurements**

3   Igor Veselovskii[1], Qiaoyun Hu[2], Philippe Goloub[2], Thierry Podvin[2], William Boissiere[2], Mikhail

4   Korenskiy[1], Nikita Kasianik[1], Sergey Khaykyn[3], Robin Miri[2]

5

6   *[1]Prokhorov General Physics Institute of the Russian Academy of Sciences, Moscow, Russia.*

7   *[2]Univ. Lille, CNRS, UMR 8518 - LOA - Laboratoire d'Optique Atmosphérique, F-59650 Lille,*

8   *France*

9   *[3]Laboratoire Atmosphère Observations Spatiales, UVSQ, CNRS, Sorbonne University,*

10 *Guyancourt, France*

11 **Correspondence**: Qiaoyun Hu (qiaoyun.hu@univ-lille.fr)

12

13 **Abstract**

14   Polarization properties of the fluorescence induced by polarized laser radiation are widely

15 considered in laboratory studies. In lidar observations, however, only the total scattered power of

16 fluorescence is analyzed. In this paper we present results obtained with a modified Mie-Raman-

17 Fluorescence lidar operated at the ATOLL observatory, Laboratoire d'Optique Atmosphérique,

18 University of Lille, France, allowing to measure depolarization ratios of fluorescence at 466 nm

19 (δ_F) and of water vapor Raman backscatter. Measurements were performed in May-June 2023

20 during Alberta forest fires season when smoke plumes were almost continuously transported over

21 the Atlantic Ocean towards Europe. During the same period, smoke plumes from the same sources

22 were also detected and analyzed in Moscow, at General Physics Institute (GPI), with a 5-channel

23 fluorescence lidar able to measure fluorescence backscattering at 438, 472, 513, 560 and 614 nm.

24 Results demonstrate that, inside the boundary layer (BL), urban aerosol fluorescence is maximal

25 at 438 nm, then it gradually decreases with wavelength. Results also show that the maximum of

26 the smoke fluorescence spectrum shifted towards longer wavelengths. The smoke layers observed

27 within 4-6 km present a maximum of fluorescence at 513 nm while, in the upper troposphere (UT),

28 the maximum shifts to 560 nm. Regarding fluorescence depolarization, its value typically varies

29 inside the 45-55 % range, however several smoke plume layers detected above 10 km were

30 characterized by a δ_F increasing up to 70%. Inside the BL, the fluorescence depolarization ratio

31 was higher than that of smoke and varied inside the 50-70% range. Moreover, in the BL, δ_F appears

32   to vary with atmospheric relative humidity (RH) and, in contrast to the elastic scattering,

33   fluorescence depolarization increases with RH.

34   The depolarization ratio of the water vapor Raman backscattering is shown to be quite low

35   (2±0.5%) in the absence of fluorescence, because the narrowband interference filter in the water

36   vapor channel selects only strongest vibrational lines of the Raman spectrum. As a result,

37   depolarization of the water vapor Raman backscattering is sensitive to the presence of strongly

38   depolarized fluorescence backscattering. The fluorescence contamination into the water vapor

39   Raman channel can be calculated from the water vapor Raman depolarization ratio with the only

40   assumption that δ_F remains constant within the 408-466 nm range.

41

42   **1. Introduction**

43   Possibility to measure the laser induced fluorescence becomes an important added-value to

44   existing Mie-Raman lidars, because fluorescence measurements provide new independent

45   information about aerosol properties. Nowadays, the spectroscopic lidars based on 32-channel

46   PMT combined with spectrograph proved the ability to measure the fluorescence spectrum

47   (Sugimoto et al., 2012; Reichardt, 2014; Reichardt et al., 2018, 2023, Liu et al., 2022). On the

48   other hand, the lidars, with a single fluorescence channel can be widespread due to their simplicity

49   (Rao et al., 2018; Veselovskii et al., 2020). Such single channel fluorescence measurements

50   combined with depolarization measurements at elastic wavelength, provide new independent

51   information about aerosol type (Veselovskii et al., 2022; Wang et al., 2023). However, in all lidar

52   studies, only total scattered power was analyzed, while polarization properties of the fluorescence

53   were ignored. At the same time, fluorescence depolarization measurements are widely used in

54   laboratory research (Lakowicz, 2006). When polarized laser radiation is used for excitation, the

55   fluorescence emission is also partly polarized and degree of emission polarization (anisotropy)

56   depends on the fluorescence lifetime, on the angle between excitation and emission dipoles, and

57   on the rotational mobility of molecules (Lakowicz, 2006). In fluorescence spectroscopy the

58   anisotropy is introduced as given by Eq.1:

59   $$r = \frac{P_F^{\parallel} - P_F^{\perp}}{P_F^{\parallel} + 2P_F^{\perp}}$$ (1)

60   Here $P_F^{\parallel}$ and $P_F^{\perp}$ are the powers of co- and cross-polarized fluorescence components. In lidar

61   measurements, however, a commonly used parameter is the depolarization ratio, δ_F.

Atmospheric
Measurement
Techniques
Discussions

62 $\quad \delta_F = \dfrac{P_F^{\perp}}{P_F^{\parallel}}$ (2)

63 Anisotropy and depolarization ratio are two interconvertible parameters

64 $\quad r = \dfrac{1-\delta_F}{1+2\delta_F}$ (3)

65   For randomly oriented fluorophores with collinear absorption and emission dipoles, in the

66 absence of rotational motion, the anisotropy is r=0.4 (Lakowicz, 2006), which corresponds to

67 δ_F=33%. This is the minimal value one can expect in lidar measurements. Existence of the angle

68 between absorption and emission dipoles, as well as molecule rotation in the process of emission

69 will increase δ_F. Thus, measurement of fluorescence depolarization ratio may bring additional

70 information about atmospheric aerosol. Moreover, depolarization measurements help to analyze

71 the impact of fluorescence on water vapor Raman measurements.

72   Water vapor is a key atmospheric component playing essential role in the planet's radiative

73 balance, and Raman lidars today are widely used for vapor observations (Whiteman, 2003, Chouza

74 et al., 2022 and references therein). However, when the UV laser beam passes through a smoke

75 layer, the broadband fluorescence signal is induced and its spectrum includes the region of water

76 vapor Raman lines. Thus, the signal in the water vapor channel (around 407.5 nm, when 354.7 nm

77 radiation is used for stimulation) becomes contaminated by the fluorescence backscatter signal

78 (Immler et al.. 2005; Immler and Schrems, 2005). This contamination can be reduced by

79 decreasing the width of the transmission band in the water vapor channel down to tenths of nm.

80 However, as it was shown recently, fluorescence still remains the issue, especially inside the smoke

81 layers in high troposphere (Chouza et al., 2022; Reichardt et al., 2023).

82   Depolarization measurements provide an opportunity to monitor the presence of

83 fluorescence signal in Raman channel. The Q-branch of water vapor Raman lines (near 407.5 nm)

84 provides a weakly depolarized backscatter, while fluorescence is strongly depolarized. Thus the

85 presence of fluorescence should increase the depolarization ratio of signal in the water vapor

86 channel. Moreover, if depolarization ratios of water vapor and fluorescence are known, the

87 contribution of fluorescence to the measured water vapor mixing ratio (WVMR) can be evaluated.

88   In this article, report and analyze, for the first time, depolarization ratio of aerosol

89 fluorescence and depolarization ratio of water vapor Raman backscatter from lidar observations

90 performed at the ATOLL observatory (ATmospheric Observation at liLLe), Laboratoire

91 d'Optique Atmosphérique, University of Lille, during dense smoke events that occurred in May -

92 June 2023. We start with a description of the experimental setup in Sect.2.1 and derive, in Sect.

93 2.2, the main equations for estimating the fluorescence contribution to the water vapor Raman

94 channel. In the first part of the results section (Sect.3.1), the fluorescence depolarization ratio over

95 ATOLL is analyzed for different aerosol types. The measurements of fluorescence spectra

96 performed with a new five-channel fluorescence lidar, operated in Moscow, are presented in

97 Sect.3.2. In Sect. 3.3, we analyze depolarization in the water vapor Raman channel and estimate

98 the contamination of fluorescence to the derived WVMR. The article ended with a conclusion.

99

100 **2. Experimental setup and data analysis**

101 *2.1 Lidar system*

102 In our study, two lidar systems were considered. The first one, LILAS ((LIlle Lidar

103 AtmosphereS) is a multiwavelength Mie-Raman-Fluorescence lidar, whereas the second one is a

104 multiwavelength fluorescence lidar operated by General Physics Institute (GPI), Moscow (Veselovskii

105 et al., 2023). Both systems are based on a tripled Nd:YAG laser (Q-Smart 450) with a 20 Hz

106 repetition rate and pulse energy about 100 mJ at 355 nm. Backscattered light in both systems is

107 collected by a 40 cm aperture telescope and the lidar signals are digitized with Licel transient

108 recorders with 7.5 m range resolution, allowing simultaneous detection in the analog and photon

109 counting mode.

110 LILAS allows the so called $3\beta+2\alpha+3\delta$ configuration, including three particle

111 backscattering (β_{355}, β_{532}, β_{1064}), two extinction (α_{355}, α_{532}) coefficients along with three particle

112 depolarization ratios. The Raman channel with 407.54/0.3 nm interference filter allows also water

113 vapor profiling. At the end 2019, the lidar was modified to enable fluorescence measurements. A

114 part of the fluorescence spectrum is selected by a wideband interference filter of 44 nm width

115 centered at 466 nm (Veselovskii et al. 2020).

116 In the fluorescence lidar of GPI only 355 nm wavelength is emitted, while fluorescence is

117 measured in five spectral intervals. The central wavelengths and widths of transmission bands are:

118 438(29), 472(32), 513(29), 560(40) and 614(54) nm (Veselovskii et al., 2023). Thus, the

119 fluorescence spectrum could be sampled. At GPI, the measurements were performed at an angle

120 of 48 deg to the horizon. The strong sunlight background restricts the fluorescence observations

121 of both systems to nighttime hours.

122   Several properties can be derived from fluorescence. The fluorescence backscattering

123   coefficient, $\beta_{F\lambda}$, at wavelength λ_F , is calculated from the ratio of fluorescence and nitrogen Raman

124   backscattering signals, as described in Veselovskii et al. (2020). We remind that $\beta_{F\lambda}$ is related to

125   fluorescence signals integrated over the filter transmission band D_λ. In Moscow measurements are

126   performed at five wavelengths, and to compare $\beta_{F\lambda}$ between different channels one makes use of

127   the "fluorescence spectral backscattering coefficient" $B_\lambda = \dfrac{\beta_{F\lambda}}{D_\lambda}$ (fluorescence backscattering per

128   spectral interval). LILAS has only one single fluorescence channel, therefore, when presenting

129   data from LILAS, for the sake of simplicity, one uses notation $\beta_{F466}=\beta_F$. The intensive property

130   characterizing aerosol fluorescence is the fluorescence capacity $G_{F\lambda}$, which is the ratio of the

131   fluorescence backscattering at wavelength λ_F to backscattering coefficient at laser wavelength

132     $G_{F\lambda} = \dfrac{\beta_F}{\beta_\lambda}$. This ratio, in principle, can be calculated for any laser wavelength. For LILAS

133   observations $G_{F\lambda}$ is calculated with respect to β_{532}, because β_{532} is derived with rotational Raman

134   scattering and is considered to be the most reliable. And again, when presenting LILAS data, for

135   simplicity one will use notation $G_{F\lambda}=G_F$. In this work, all profiles of aerosol properties are

136   smoothed with the Savitzky – Golay method, using second order polynomials with 8 points in the

137   window.

138   Additional information about the atmospheric thermodynamic state was available from

139   radiosonde measurements performed at Herstmonceux (UK) and Beauvechain (Belgium) stations,

140   located 160 km and 80 km away from the ATOLL observatory respectively. When calculating the

141   relative humidity, one then used the water vapor profiles measured by Raman lidar and temperature

142   profiles provided by the radiosonde.

143   As discussed in the introduction, measurements of fluorescence depolarization ratio and

144   depolarization of water vapor Raman backscatter are expected to bring new information about

145   aerosol properties and fluorescence contamination in the water vapor Raman channel. In 2023,

146   LILAS was upgraded to allow depolarization measurements at both 466 nm and 408 nm.

147   Corresponding optical layout is shown in Fig.1. Dichroic mirrors DM separate 387, 408 and 466

148   nm components, while polarizing cubes split the components with polarizations oriented parallel

149   (s) and perpendicular (p) to the laser polarization. For both channels the polarizing cube PBS251

150   from ThorLabs was used. Fluorescence depolarization ratio, δ_F , and water vapor Raman scattering

Atmospheric
Measurement
Techniques
Discussions
Open Access
EGU

151 depolarisation ratio, δw , are both defined and calculated as a ratio of the perpendicular to the

152 parallel respective components. Calibration was performed as described in Freudenthaler et al.

153 (2009). The uncertainty of calibration is estimated to be below 15% for both 466 and 408 nm

154 channels.

155

156 **2.2 Expressions for estimating fluorescence impact on water vapor measurements**.

157 As discussed in the recent work from Chouza et al. (2022) and Reichardt et al. (2023), the

158 broadband aerosol fluorescence is expected to contribute to the signal measured in water vapor

159 Raman channel. Below, one provides the basic equations for estimating this contribution, based

160 on the measurements of the depolarization ratio in the water vapor Raman channel. The

161 backscattered radiative power, at the laser wavelength λ_L, from distance z, can be modeled, after

162 background subtraction, by

163 $$P_L = O(z)\frac{1}{z^2}C_L\beta T_L^2 \qquad (4)$$

164 Here $O(z)$ is the geometrical overlap factor, which is assumed to be the same for all channels. C_L

165 is the range independent constant, including efficiency of the detection channel. T_L is one-way

166 transmission, describing light losses on the way from the lidar to distance z at wavelength λ_L.

167 $$T_L = \exp\left\{-\int_0^z [\alpha^a(\lambda_L, z') + \alpha^m(\lambda_L, z')]dz'\right\} \qquad (5)$$

168 Backscattering and extinction coefficients contain aerosol (a) and molecular (m) contributions:

169 $$\beta_{\lambda_L} = \beta_{\lambda_L}^a + \beta_{\lambda_L}^m \text{ and } \alpha_{\lambda_L} = \alpha_{\lambda_L}^a + \alpha_{\lambda_L}^m .$$

170 Radiative power in nitrogen Raman, water vapor Raman, and fluorescence channels can be

171 written in a similar way.

172 $$P_R = O(z)\frac{1}{z^2}C_R\sigma_R N_R T_L T_R \qquad (6)$$

173 $$P_W = O(z)\frac{1}{z^2}C_W N_W \sigma_W T_W T_L \qquad (7)$$

174 $$P_F = O(z)\frac{1}{z^2}C_F\beta_F T_F T_L \qquad (8)$$

175 Here C_R, C_W, C_F are the corresponding range independent constants. Terms $T_R, T_V,$ and T_F are one-

176 way transmissions at wavelengths $\lambda_R, \lambda_W, \lambda_F$, corresponding to the centers of transmission bands of

177 the channels. Terms N_R and N_W are the concentrations in nitrogen and water vapor molecules while

178 σ_R, σ_W are their Raman differential scattering cross sections respectively. The fluorescence

179 backscattering coefficient, β_F, is introduced the same way, as described in (Veselovskii et al.,

180 2020).

181 The power of fluorescence signal that leaks to the water vapor channel is:

182
$$P_{FW} = O(z)\frac{1}{z^2}C_W\beta_{FW}T_W T_L \tag{9}$$

183 Here β_{FW} is fluorescence backscattering at wavelength λ_W. The WVMR, n_W, can be obtained from

184 Eq.6 and Eq.7, if the calibration constant $K_W = \dfrac{C_R}{C_W}\dfrac{\sigma_R}{\sigma_W}$ is known and is given by Eq. 10

185
$$n_W = K_W \frac{P_W}{P_R}\frac{T_R}{T_W} \tag{10}$$

186 The fluorescence backscattering coefficient, β_F, derived from Eq.6 and Eq.8, also contains

187 the calibration constant K_F. The procedure of calibration is described in Veselovskii et al. (2020).

188 Finally, β_F is given by Eq. 11.

189
$$\beta_F = K_F n_R \frac{P_F}{P_R}\frac{T_R}{T_F} \tag{11}$$

190 Here $n_R = \dfrac{N_R(z)}{N_R(z=0)}$ is relative change of number density of nitrogen molecules with height.

191 The fluorescence signal in the water vapor channel can be expressed from P_F using parameter η,

192 which depends on ratio of fluorescence cross sections at wavelengths λ_W and λ_F, on the filters

193 width and on efficiency of both channels.

194
$$P_{FW} = P_F \eta \frac{T_W}{T_F} \tag{12}$$

195 The signal measured in the water vapor channel, $\tilde{P}_W$, is the addition of both water vapor

196 backscatter, P_W, and the fluorescence backscatter, P_{FW},

197
$$\tilde{P}_W = P_W + P_{FW} = P_W + P_F \eta \frac{T_W}{T_F} \tag{13}$$

198 One should remember, that the fluorescence spectrum, even for the same type of aerosol, can vary

199 with altitude and from observation to observation, which influences η. To minimize this influence

200 it is desirable to keep λ_W and λ_F as close as possible.

201   If the signals in the water vapor Raman and fluorescence channels are separated into co-

202   polarized (II) and cross-polarized ($\perp$) components, in respect to laser polarization state, their

203   powers in water vapor Raman channel are given respectively by Eq. 14 and Eq. 15

$$\tilde{P}_W^{\parallel} = P_W^{\parallel} + P_F^{\parallel}\eta\frac{T_W}{T_F} \tag{14}$$

$$\tilde{P}_W^{\perp} = P_W^{\perp} + P_F^{\perp}\eta\frac{T_W}{T_F} = \delta_W P_W^{\parallel} + \delta_F P_F^{\parallel}\eta\frac{T_W}{T_F} \tag{15}$$

206   Here δ_F and δ_W are the fluorescence and water vapor Raman depolarization ratios, defined in Eq.16

$$\delta_F = \frac{P_F^{\perp}}{P_F^{\parallel}} \qquad \delta_W = \frac{P_W^{\perp}}{P_W^{\parallel}} \tag{16}$$

208   Here we assume that depolarization ratio of fluorescence is the same at the wavelengths λ_W and

209   λ_F. This assumption is usually valid, because emission is normally from the lowest singlet state,

210   so the depolarization ratio is spectrally independent (Lakowicz, 2006).

211   Due to the presence of fluorescence, the depolarization ratio measured in the water vapor

212   Raman channel is given by Eq.17

$$\tilde{\delta}_W = \frac{\tilde{P}_W^{\perp}}{\tilde{P}_W^{\parallel}} = \frac{\delta_W P_W^{\parallel} + \delta_F P_F^{\parallel}\eta\frac{T_W}{T_F}}{P_W^{\parallel} + P_F^{\parallel}\eta\frac{T_W}{T_F}} \tag{17}$$

214   Here δ_W is the depolarization ratio that would be measured in the water vapor Raman channel in

215   the absence of atmospheric fluorescence. From Eq.9, 10, 14, 15, 17 parameter η can be derived

216   from lidar measurements, such as water vapor mixing ratio, $\tilde{n}_V$, depolarization ratio $\tilde{\delta}_W$ and

217   fluorescence backscattering β_F :

$$\eta = \frac{\tilde{n}_W}{\beta_F}\frac{K_F}{K_W}n_R\frac{(1+\delta_F)(\tilde{\delta}_W - \delta_W)}{(1+\tilde{\delta}_W)(\delta_F - \delta_W)} \tag{18}$$

219   It should be note, that the choice of calibration constants K_F, K_W does not influence η, because $\tilde{n}_W$

220   and β_F are calculated with the same calibration constants. Finally, the increase of WVMR Δn_W

221   induced by the fluorescence can be calculated following Eq.19:

222
$$\Delta n_W = K_W \frac{P_F \eta \dfrac{T_W}{T_F}}{P_R} \frac{T_R}{T_W} = \frac{K_W}{K_F} \eta \beta_F \frac{1}{n_R} \tag{19}$$

223   As soon as parameter η is found from Eq.18, we can estimate error Δn_W from β_F, which in

224 case of LILAS is measured at 466 nm. In such estimation we have to assume that relationship

225 between fluorescence at 466 nm and 408 nm is constant (independent of height). Possibility to

226 perform correction from single – channel fluorescence measurements was discussed by Reichardt

227 et al. (2023), where it was shown, that for 466/408 nm channels, correction actually may depend

228 on height. Corresponding analysis based on our measurements will be presented in Sect.3.2.

229   We should mention, that when depolarization of water vapor Raman is available, the

230 contribution of fluorescence to WVMR can be obtained without using η. From Eq.18 and Eq.19 it

231 comes:

232
$$\Delta n_W = \tilde{n}_W \frac{(1+\delta_F)\left(\tilde{\delta}_W - \delta_W\right)}{(1+\tilde{\delta}_W)\left(\delta_F - \delta_W\right)} \tag{20}$$

233 However, such correction can be performed only at low altitudes, where signal-to-noise ratio in

234 cross-polarized water vapor channel is high enough.

235

236 **3. Experimental results**

237   In May – June 2023, the Canadian forest fires were at the origin of numerous smoke layers

238 observations in a wide range of altitude, ranging from the BL to the tropopause. The Boreal

239 wildfire season in 2023 started anomalously early. A wildfire in Alberta, Canada at 53.2° N, 115.7°

240 W has produced an intense Pyrocumulonimbus (PyroCb) cloud on 5 May with the minimum

241 satellite-derived infrared brightness temperature of -66° C, which should correspond to 10-11 km

242 altitude according to the local radiosoundings. In order to describe the long-range transport of the

243 smoke plume produced by this event, we use UV absorbing Aerosol Index (AI) measurements by

244 the Ozone Monitoring and Profiling Suite (OMPS) Nadir Mapper (NM) instrument onboard Suomi

245 NPP satellite mission (Flynn et al., 2014). AI is widely used as a proxy of the amount of absorbing

246 aerosols (e.g smoke, dust, ash) and its dimensionless value is proportional to the altitude of the

247 aerosol layers. The AI values above 15 are usually associated with the smoke plumes at or above

248 the tropopause (Peterson et al., 2018 and references therein), whereas the maximum AI value

249 reported by OMPS-NM instrument for the Alberta event amounted to 19.9.

Atmospheric
Measurement
Techniques
Discussions

Open Access

EGU

250   Fig. 2 displays the spatiotemporal evolution of the smoke plume from the Alberta event

251   represented by the areas of enhanced AI observed between 5 – 21 May. The smoke in the upper

252   troposphere and lower stratosphere (UTLS) is carried by the westerly winds, crossing the Atlantic

253   in about 1 week before reaching Moscow region by 15 May. On that date, the Moscow lidar has

254   detected the smoke layer at 10-11 km (see Sect. 2). The plume was then further advected across

255   Eurasia towards northeastern Siberia. By 22 May the smoke plume completes its first

256   circumnavigation (not shown) and passes over Lille on 23 May and then over Moscow for the

257   second time around 27 May. Thus, we can expect, that the smoke layers observed over Lille and

258   Moscow have the same source.

259

260   ### 3.1 Variability of fluorescence depolarization ratio

261   At the first stage of our research we focused on the variability of the fluorescence

262   depolarization ratio with aerosol types. The main attention was paid to smoke particles, because

263   they provide the strongest impact on the Raman water vapor measurements due to their high

264   fluorescence capacity.

265   Spatio-temporal distributions of the aerosol elastic and fluorescence backscattering

266   coefficients (β_{532} and β_F), on the night 26-27 June 2023, are shown in Fig.3. Dense smoke layer

267   with β_F as high as 7.0×10^{-4} Mm^{-1}sr^{-1} occurs within the 4.0 -10.0 km height range. The relative

268   humidity increases from 40% at 4 km to RH>90% at 7 km where formation of ice crystals starts.

269   Vertical profiles of aerosol elastic and fluorescence backscattering coefficients (β_{532} and β_F),

270   together with fluorescence capacity, are shown in Fig.3c. Inside the smoke layer, G_F is about 3×10^{-4},

271   which is a typical value for smoke whereas, above 6 km, it decreases due to ice formation. Ice

272   crystals increase the particle depolarization ratio δ_{532} from 3% at 6 km to 20% at 8 km.

273   Fluorescence signals are strongly depolarized. Inside the BL, δ_F is about 60% whereas above 2 km

274   it drops to approximately 45%. The processes of hygroscopic growth and ice formation do not

275   provide a noticeable impact on δ_F value. During May – June observations, the depolarization ratio

276   of smoke varied mainly inside the 45-55% range.

277   As discussed in our previous publications (Veselovskii, et al., 2022; Hu et al., 2022), the

278   fluorescence capacity of aged smoke varies inside the $(2.5-5.5) \times 10^{-4}$ range, probably due to the

279   changes in smoke composition and conditions of atmospheric transport. However, during Alberta

280   fires, several smoke plumes with high G_F have been observed. The highest fluorescence capacity

281   was observed on the night 16-17 June 2023. Vertical profiles of aerosol properties for this episode

282   are shown in Fig.4. Dense smoke layers with fluorescence backscattering exceeding 10.0×10^{-4}

283    $Mm^{-1}sr^{-1}$ occurred within 7.0 -9.0 km height range. In this case, the maximal value of fluorescence

284   capacity reached 10.0×10^{-4}. Fluorescence depolarization ratio is about 50% through the entire

285   smoke layer and the process of ice formation (just like in Fig.3d) does not influence δ_F. Thus, in

286   May - June 2023 strong variations of G_F in the $(2.5-10.0) \times 10^{-4}$ range were accompanied by

287   relatively small variations of δ_F remaining in the 45 - 55% interval.

288   It is known that in the UTLS smoke particles can reach depolarization ratio, δ_{532} , as high as

289   15-20% (Burton et al., 2015; Haarig et al., 2018; Hu et al., 2019; Ohneiser et al., 2020). High

290   values of the depolarization ratio are usually attributed to the complex internal structure of smoke

291   particles (Mishchenko et al., 2016). Two smoke events in the UTLS, characterized by enhanced

292   δ_{532}, on 28-29 May and 3-4 June 2023, are illustrated on Fig.5. On 28-29 May, three smoke layers,

293   at ~ 3.5, 6.5 and 11.5 km can be distinguished. High depolarization ratios, reaching 40% at altitudes

294   of 9.8-10.5 km, are due to ice clouds. In the lower smoke plumes ranging between 3.5 and 6.5 km,

295   the particle depolarization did not exceed 8% whereas above 11 km δ_{532} increases to 15%. High

296   values of δ_{532} observed in the UTLS correlate with increase of G_F and with fluorescence

297   depolarization, δ_F, up to 7.0×10^{-4} and 70% respectively. Similar behavior was observed on 3-4

298   June, where depolarization ratio, δ_{532}, above 11.5 km increased up to 15%, simultaneously with an

299   increase of G_F and δ_F up to 9.5×10^{-4} and 70% respectively. Thus, change in particle morphology

300   may affect the depolarization ratio of fluorescence. Another possibility is that, in the UTLS, not

301   only the particle structure can change, but composition as well. At the current stage of analysis,

302   we are not yet able to conclude about the mechanisms explaining the increase of fluorescence

303   depolarization in the UTLS.

304   We did not observe the effect of atmospheric humidity on smoke fluorescence

305   depolarization. However, inside the BL the observed hygroscopic growth was accompanied by an

306   increase of δ_F. During the 9-16 June 2023 period numerous particle hygroscopic growth cases were

307   observed in the BL. One of such cases, on the night of 12-13 June, is shown in Fig.6. The relative

308   humidity increases inside the BL from 50% to 70% causing an increase of β_{532} near the BL top.

309   Depolarization ratio δ_{532} decreases with height, since the particles in the process of hygroscopic

310   growth become more spherical. The fluorescence depolarization ratio, however, increases inside

311   the boundary layer from 50 to 70%.

312   All results obtained during 9-16 June, showing dependence of δ_F and δ_{532} on the relative

313   humidity, are summarized in Fig.7. Particle depolarization δ_{532} systematically decreased with RH

314   but, on 16 June, this dependence is not monotonic which could be due to the change of aerosol

315   composition with height. At low RH (below 30%), fluorescence depolarization ratio is about 50%.

316   However, at RH about 90%, δ_F increases up to 70%. One possible explanation of δ_F behavior can

317   be an increase of rotational mobility of the molecules in the process of particle water uptake.

318

319   *3.2 Fluorescence spectrum sampled with a with 5-channel lidar*

320   The results presented in the previous section were obtained with a single channel

321   fluorescence lidar. However, for analyzing the variability of smoke properties (for example,

322   increase of fluorescence capacity with height) it is important to have information about total

323   fluorescence spectrum. Moreover, to estimate the fluorescence contamination in the Raman water

324   vapor channel, a relationship between fluorescence backscattering at 466 nm and 408 nm is used.

325   Thus we need to know the variability of the fluorescence spectrum in the short wavelength region.

326   In our recent work (Veselovskii et al., 2023) we presented the first results obtained with a 5-

327   channel fluorescence lidar in operation at the GPI. This lidar is able to measure fluorescence

328   backscattering in 5 spectral intervals centered at 438, 472, 513, 560, and 614 nm. In May – June

329   2023, several smoke plumes originating from Alberta fires were transported over Moscow.

330   Although Lille and Moscow are very distant from each other, smoke plumes observed have the

331   same origin, hence the fluorescence spectra measured over Moscow are quite helpful for the

332   analysis of Lille data.

333   Fig.8 presents fluorescence spectral backscattering coefficients, B_λ, for 3 smoke events

334   detected in the UTLS above 10, 8 and 10 km for 15, 31 May and 20 June 2023, respectively. On

335   15 and 31 May smoke layers are also present inside the 4-6 km range. Inside the BL the strongest

336   fluorescence is systematically detected in the 438 nm channel while, at higher altitudes, the

337   maxima shifts to 560 nm. As follows from Fig.8d-f, the ratio B_{560}/B_{438} remains in the range 0.4 -

338   0.7 inside the BL whereas this ratio increases above 2.0 in the UTLS. Thus, for smoke events the

339   maxima of the fluorescence spectrum shifts with height towards longer wavelengths. The ratio

340   B_{513}/β_{355} also increases with height and, above 10 km, it reaches the values of 1×10^{-5} nm^{-1}. In the

341   UTLS, the maximal fluorescence capacity, G_F, measured by LILAS at 466 nm (with 44 nm

342   bandwidth filter) was about 10×10^{-4}. In the smoke layer, the ratio of backscattering coefficients

343   β_{355}/β_{532} is about 2, so the maximal ratio B_{466}/β_{355} derived from LILAS measurements is about

344   1.1×10^{-5} nm^{-1}. Thus, values obtained over Lille and over Moscow are in agreement.

345   The fluorescence spectra obtained for the above mentioned smoke plumes are shown in

346   Fig.9. The values of B_{λ} are normalized to B_{438}. Inside the BL, the maximum of fluorescence is

347   measured at 438 nm and it decreases with wavelength. In the smoke layers within 4 - 6 km, the

348   maximum of fluorescence is observed at 513 nm while, in the UTLS, the maximum shifts to 560

349   nm.

350   When applying Eq.19 to estimate the contribution of smoke fluorescence into the Raman

351   water vapor channel of LILAS, we assume that the ratio of the fluorescence backscattering at 466

352   nm to 408 nm is constant. For the lidar in operation at GPI, the shortest available wavelength is

353   438 nm, therefore, at least, one can estimate the variability of the ratio B_{472}/B_{438}. Fig. 10 presents

354   vertical profiles of B_{472}/B_{438} for 11 smoke events occurring during the 15 May – 20 June 2023

355   period. Inside the BL, this ratio varies in the 0.6 – 1.0 range. Lowest values correspond to urban

356   aerosols while, values of B_{472}/B_{438} close to 1.0, probably indicate the presence of smoke particles

357   inside the BL. Smoke layers start mainly above 4.0 km and B_{472}/B_{438} shows a tendency to increase

358   in the UT. It is interesting that, for the period 15 May – 1 June, the ratio was close to 1.5 whereas

359   after 1 June, it became close to 1.0, which can be related to changing of smoke source. Mean value

360   of B_{472}/B_{438} in the 4.0 – 11.0 km range over all observations is 1.38 with standard deviation of 0.23

361   (relative variation is about 17%). The wavelength separation between 466 nm and 408 nm channels

362   is 1.7 larger, so one can expect variation of B_{466}/B_{408} in the smoke layer up to ~30%. This is a very

363   rough estimation, but it points out the difficulties to face when the estimation of the fluorescence

364   contamination to the Raman water vapor channel is performed from a single fluorescence channel

365   at 466 nm. This issue was also discussed in the publication of Reichardt et al. (2023).

366

367   *3.3 Estimation of fluorescence impact on water vapor Raman measurements*

368   Measuring the depolarization ratio in the water vapor Raman channel provides an

369   opportunity to control/evaluate the presence of fluorescence leak in this channel. These

370   depolarization measurements were performed in Lille during May – June 2023. Vertical profiles

371   of water vapor depolarization ratio $\tilde{\delta}_W$ together with $\tilde{n}_W$, β_{532}, β_F, and G_F are shown in Fig.11 for

372   the night 8-9 and 10-11 June 2023. On 8-9 June aerosols are confined mainly below 5 km. The

373   fluorescence capacity is about 1.0×10^{-4} below 3.0 km, but above, G_F increases up to 2.5×10^{-4},

374   indicating to the presence of smoke. The depolarization ratio in the water vapor channel is about

375   2% in the height range 1.5 km – 3.5 km. The values of $\tilde{\delta}_W$ ranging inside 1.8%÷2.0% were

376   observed for this height range, where contribution of fluorescence was insignificant.

377   Depolarization ratio δ_W is low, because the interference filter in water vapor channel selects only

378   strongest Q-branch lines and most of rotational lines are blocked. Contribution of fluorescence

379   becomes noticeable above 3.5 km where n_W drops, resulting in an increase of $\tilde{\delta}_W$ up to ~3%. There

380   is also increase of $\tilde{\delta}_W$ up to 2.2% below 1.0 km, where fluorescence backscattering is enhanced.

381   Similar values of $\tilde{\delta}_W$ were observed on 10-11 June, where depolarization ratio increases up to

382   2.5% inside the smoke layer observed at ~3.75 km and below 2.0 km.

383   As discussed in section 2.2, the contribution of fluorescence to the WVMR can be derived

384   from Eq.20 if $\tilde{\delta}_W$ and δ_F are measured. Fig.12 presents the modeling of the relative error $\frac{\Delta n_W}{\tilde{n}_W}$,

385   introduced by the fluorescence to WVMR as a function of $\tilde{\delta}_W$. Computations are performed for

386   fluorescence depolarization ratio δ_F=50%, 60%, 70% to include both smoke and urban particles.

387   Depolarization ratio in the Raman water vapor channel in the absence of fluorescence was assumed

388   to be δ_W=2%. For depolarization ratio $\tilde{\delta}_W$ below 3% the relative error $\frac{\Delta n_W}{\tilde{n}_W}$ did not exceed 3%.

389   As follows from the fluorescence spectra in Fig.9, the fluorescence of urban particles increases

390   towards short wavelengths, thus one can expect impact of the urban aerosol fluorescence on vapor

391   measurement. In practices, however, we did not observe $\tilde{\delta}_W$ exceeding 3% in the BL thus,

392   contribution of aerosol in the BL is not critical. The reason is due to the low fluorescence capacity

393   (about one order lower than that of smoke) and higher water vapor content, comparing to free

394   troposphere.

395   Profiles of $\tilde{\delta}_W$ shown in Fig.11 become noisy at heights where n_W is low, and $\tilde{\delta}_W$ can not be

396   used for correction of fluorescence effect in the UT. To overcome this, one derived the parameter

397   η from Eq.18 at low altitudes where $\tilde{\delta}_W$ is available, and, then, this η is used to calculate Δn_W from

398   Eq.19 in the entire height range. In such an approach, however, one has to assume that relationship

399   between fluorescence cross sections at 466 nm and 408 nm remains constant with height. As

400 discussed in previous section, such assumption can yield significant bias in calculation of Δn_W,

401 and, at this stage, we do not provide corrected profiles of WVMR.

402 For accurate calculation of η one needs smoke events with strongly enhanced $\tilde{\delta}_W$, which is

403 usually observed in the dry smoke layers. Such suitable events are shown for the night 26-27 May

404 and 5-6 June 2023 in Fig.13. On 26-27 May a smoke layer characterized by high fluorescence (β_F

405 up to 5×10^{-4} Mm^{-1}sr^{-1}) and low $\tilde{n}_W$ (below 0.2 g/kg) is observed at 3.5 km. Fluorescence

406 depolarization ratio is about 47% and $\tilde{\delta}_W$ increases from 2% up to 12% in the middle of this layer.

407 Parameter η calculated from Eq.18 inside this smoke layer is about 2×10^{-3} (g/kg)/(Mm^{-1}sr^{-1}). On

408 5-6 June the depolarization ratio $\tilde{\delta}_W$ in the smoke layer increased up to 10% and value of η is very

409 similar. Parameters η derived for several smoke episodes vary in the range $(2 \div 2.5) \times 10^{-3}$

410 (g/kg)/(Mm^{-1}sr^{-1}). For the estimate of Δn_W one used the mean value of $\eta = 2.25 \times 10^{-3}$ (g/kg)/(Mm^{-1}

411 ^{1}sr^{-1}), which is suitable only for smoke, while for particles in the BL, η can be different. However,

412 in the BL, low depolarization ratio $\tilde{\delta}_W$ prevented us from calculating η.

413 Fig.14 presents vertical profiles of WVMR, fluorescence backscattering and error Δn_W

414 introduced by the fluorescence in WVMR on 26-27 May, 28-29 May and 16-17 June. Smoke layers

415 with strong fluorescence occurred systematically in our UT observations. The current LILAS

416 system is not powerful enough for deriving accurate water vapor measurements above 10 km,

417 however increase of $\tilde{n}_W$ in fluorescent smoke layers is visible. We remind that Eq.19 for Δn_W

418 contains factor $\dfrac{1}{n_R}$ (inverse relative change of nitrogen number density), thus the fluorescence

419 impact on WVMR increases with height. The uncertainties $\dfrac{\Delta n_W}{\tilde{n}_W}$ for all events considered are

420 shown in Fig.14d. On 26-27 and 28-29 May the uncertainty at 11 km is of the order of 100%. On

421 16 June the smoke layer is lower (at 9 km) and the uncertainty is about 50%. Our demonstration

422 shows that smoke fluorescence can significantly impact water vapor measurements. The proposed

423 approach, based on the analysis of the depolarization ratio of the water vapor signal, has potential

424 for estimation of corresponding errors and their correction.

425 **4. Conclusion**

426   Modern fluorescence spectroscopy widely uses depolarization measurements of the

427   fluorescence emission induced by polarized laser radiation. However, in application to lidar

428   atmospheric observations, measurement of fluorescence depolarization ratio, presented in this

429   study, is one of the first efforts in this direction. Analysis of more than 30 spring and summer

430   smoke events allows evaluation of the main aerosol intensive properties, including fluorescence

431   capacity, particle and fluorescence depolarization ratio. The fluorescence capacity varied within

432       $(2.5 \div 10.0) \times 10^{-4}$ range while the particle depolarization ratio δ_{532} remained below 10%. However,

433   in spite of strong G_F variation, δ_F was remaining within a relatively narrow interval 45-55%.

434   Additional observations revealed that for smoke plumes in the upper troposphere δ_{532} increased up

435   to 15% and fluorescence depolarization increased up to 70%. At the moment, one cannot fully

436   explain the mechanism responsible for this δ_F increase. It can be related to complex particle

437   internal structure at high altitudes, as well as to the change of the chemical composition, revealed

438   by the shift of the maximum of fluorescence spectra to longer wavelengths in the upper troposphere

439   (Fig. 9).

440   Inside the BL, the fluorescence depolarization ratio was higher than that of smoke and varied

441   inside the 50-70% range. Moreover, fluorescence depolarization ratio of urban particles strongly

442   depends on the relative humidity and, in contrast to elastic scattering, depolarization of

443   fluorescence increases with RH. One possible origin of this phenomena could be attributed to an

444   increase of rotational mobility of the molecules involved in the process of water uptake since δ_F

445   increases when rotation time of molecules becomes comparable with time of fluorescence

446   emission.

447   The depolarization ratio of Raman water vapor backscatter, in the absence of fluorescence,

448   appears to be quite low ($\delta_W=2\pm0.5\%$), because the narrowband interference filter in the water vapor

449   channel selects only strong Q-lines of the Raman spectrum. As a result, the depolarization ratio of

450   Raman water vapor backscatter is sensitive to the presence of strongly depolarized fluorescence

451   signals. Contribution of fluorescence to the WVMR can be calculated from $\tilde{\delta}_W$ with the only

452   assumption that δ_F remains constant within 408 - 466 nm. However, the depolarization ratio of

453   Raman water vapor backscatter is weak and measurements are only possible up to the middle

454   troposphere with the lidar used in the work, while the problem of fluorescence interference is the

455   most crucial in UTLS. To solve this problem, one can derive η, a parameter linking fluorescence

456 at 466 nm and at 408 nm. This parameter is calculated for specific smoke events, at low altitudes,

457 and then is used for processing all observations and altitudes.

458 Such an approach relies on the assumption that the ratio of fluorescence between 466 nm

459 and 408 nm remains constant and allows only a rough estimation of the correction term for the

460 water vapor mixing ratio, Δn_W. One possible solution to improve accuracy of Δn_W is to implement

461 an additional and shorter wavelength channel (438 nm or even shorter). Another technical solution

462 could be considered as the depolarization ratio of Raman water vapor backscatter is low, therefore

463 the 408 nm component can be efficiently selected with a polarizing cube. The depolarized channel

464 then can be used for fluorescence measurements. Polarizing cube works in a wide spectral range,

465 so one can select the region outside of the water vapor spectrum (400 nm – 418 nm) for

466 fluorescence monitoring. We plan this experiment as well as other innovative approaches with our

467 future high power fluorescence lidar, LIFE (Laser Induced Fluorescence Explorer), whose start of

468 operation is scheduled at the beginning of 2024.

469

470 *Data availability*. Lidar measurements are available upon request
471 (philippe.goloub@univ-lille.fr).

472

473 *Author contributions*. IV processed the data and wrote the paper. QH and TP performed the
474 measurements in Lille. PG supervised the project and helped with paper preparation. WB modified
475 LILAS for polarization measurements. MK and NK performed the measurements in Moscow. SK
476 analyzed transport of smoke layers and RM derived RH profiles from lidar measurements.
477 .

478 *Competing interests*. The authors declare that they have no conflict of interests.

479

480 **Acknowledgement**

489

References

491

492 Burton, S.P., Hair, J.W., Kahnert, M., Ferrare, R.A., Hostetler, C.A., Cook, A.L., Harper, D.B.,
493   Berkoff, T.A., Seaman, S.T., Collins, J.E., Fenn, M.A., and Rogers, R.R.: Observations of the
494   spectral dependence of linear particle depolarization ratio of aerosols using NASA Langley
495   airborne High Spectral Resolution Lidar, Atmos. Chem. Phys., 15, 13453–13473,
496   https://doi.org/10.5194/acp-15-13453-2015, 2015.

497 Chouza, F., Leblanc, T., Brewer, M., Wang, P., Martucci, G., Haefele, A., Vérèmes, H., Duflot,
498   V., Payen, G., and Keckhut, P.: The impact of aerosol fluorescence on long-term water vapor
499   monitoring by Raman lidar and evaluation of a potential correction method, Atmos. Meas.
500   Tech., 15, 4241–4256, https://doi.org/10.5194/amt-15-4241-2022, 2022.

501 Flynn, L., Long, C., Wu, X., Evans, R., Beck, C. T., Petropavlovskikh, I., McConville, G.,
502   Yu, W., Zhang, Z., Niu, J., Beach, E., Hao, Y., Pan, C., Sen, B., Novicki, M., Zhou, S., Seftor,
503   C.: Performance of the Ozone Mapping and Profiler Suite (OMPS) products, J. Geophys. Res.
504   Atmos., 119, 6181–6195, 2014. doi:10.1002/2013JD020467

505 Freudenthaler,V., Esselborn, M.,Wiegner, M.,Heese, B., Tesche, M. and co-authors:
506   Depolarization ratio profiling at severalwavelengths in pure Saharan dust during SAMUM
507   2006, *Tellus* 61B, 165–179, 2009.

508 Haarig, M., Ansmann, A., Baars, H., Jimenez, C., Veselovskii, I., Engelmann, R., and Althausen,
509   D.: Depolarization and lidar ratios at 355, 532, and 1064 nm and microphysical properties of
510   aged tropospheric and stratospheric Canadian wildfire smoke, Atmos. Chem. Phys., 18, 11847-
511   11861, https://doi.org/10.5194/acp-18-11847-2018, 2018.

512 Hu, Q., Goloub, P., Veselovskii, I., Bravo-Aranda, J.-A., Popovici, I. E., Podvin, T., Haeffelin,
513   M., Lopatin, A., Dubovik, O., Pietras, C., Huang, X., Torres, B., and Chen, C.: Long-range-
514   transported Canadian smoke plumes in the lower stratosphere over northern France, Atmos.
515   Chem. Phys., 19, 1173-1193, 2019. https://doi.org/10.5194/acp-19-1173-2019.
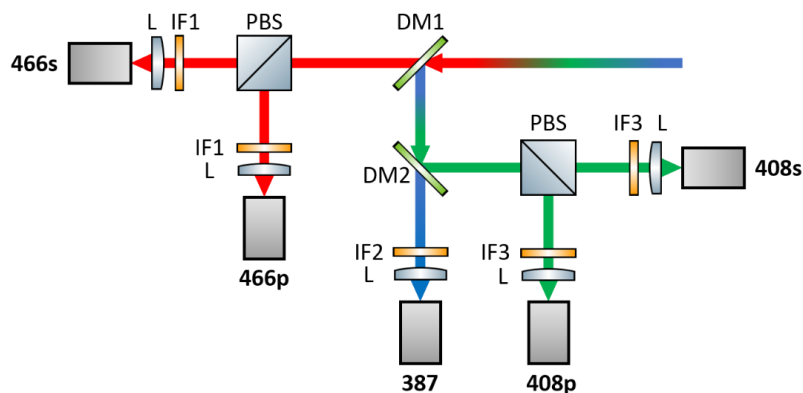
516 Hu, Q., Goloub, P., Veselovskii, I., and Podvin, T.: The characterization of long-range transported
517   North American biomass burning plumes: what can a multi-wavelength Mie-Raman-
518   polarization-fluorescence lidar provide? Atmos. Chem. Phys. 22, 5399–5414, 2022
519   https://doi.org/10.5194/acp-22-5399-2022

520 Immler, F. and Schrems, O.: Is fluorescence of biogenic aerosols an issue for Raman lidar
521   measurements? Proc. SPIE 5984, Lidar Technologies, Techniques, and Measurements for
522   Atmospheric Remote Sensing, 59840H, https://doi.org/10.1117/12.628959, 2005.

523 Immler, F., Engelbart, D., and Schrems, O.: Fluorescence from atmospheric aerosol detected by a
524   lidar indicates biogenic particles in the lowermost stratosphere, Atmos. Chem. Phys., 5, 345–
525   355, https://doi.org/10.5194/acp-5-345-2005, 2005.

526 Lakowicz, J. R.: Principles of Fluorescence Spectroscopy, Springer New York, NY, 2006.
527   https://doi.org/10.1007/978-0-387-46312-4

528 Liu, F., Yi, F., He, Y., Yin, Z., Zhang, Y., and Yu, C.: Spectrally Resolved Raman Lidar to
529   Measure Backscatter Spectra of Atmospheric Three-Phase Water and Fluorescent Aerosols
530   Simultaneously: Instrument, Methodology, and Preliminary Results, IEEE Transactions on
531   Geoscience and Remote Sensing, 60, 5703013, 2022, doi: 10.1109/TGRS.2022.3166191

532 Mishchenko MI, Dlugach JM, Liu L. Linear depolarization of lidar returns by aged smoke
533   particles. Appl Opt. 55, 9968-9973, doi: 10.1364/AO.55.009968, 2016.

534 Ohneiser, K., Ansmann, A., Baars, H., Seifert, P., Barja, B., Jimenez, C., Radenz, M., Teisseire,
535   A., Floutsi, A., Haarig, M., Foth, A., Chudnovsky, A., Engelmann, R., Zamorano, F., Bühl,
536   J., and Wandinger, U.: Smoke of extreme Australian bushfires observed in the stratosphere
537   over Punta Arenas, Chile, in January 2020: optical thickness, lidar ratios, and depolarization
538   ratios at 355 and 532 nm, Atmos. Chem. Phys., 20, 8003–8015, https://doi.org/10.5194/acp-
539   20-8003-2020, 2020.

540 Peterson, D.A., Campbell, J.R., Hyer, E.J. et al. Wildfire-driven thunderstorms cause a volcano-
541   like stratospheric injection of smoke, npj Clim. Atmos. Sci. 1, 30, 2018.
542   https://doi.org/10.1038/s41612-018-0039-3

543 Rao, Z., He, T., Hua D, Wang, Y., Wang, X., Chen, Y., Le J.: Preliminary measurements of
544   fluorescent aerosol number concentrations using a laser-induced fluorescence lidar, Appl. Opt.
545   57, 7211-7215, https://doi.org/10.1364/AO.57.007211, 2018.

546 Reichardt, J.: Cloud and aerosol spectroscopy with Raman lidar, J. Atmos. Ocean. Tech., 31,
547   1946–1963, https://doi.org/10.1175/JTECH-D-13-00188.1, 2014.

548 Reichardt, J., Leinweber, R., Schwebe, A.: Fluorescing aerosols and clouds: investigations of co-
549   existence, EPJ Web Conf., 176, 05010, https://doi.org/10.1051/epjconf/201817605010, 2018.

550   Reichardt, J., Behrendt, O., and Lauermann, F.: Spectrometric fluorescence and Raman lidar:
551   absolute calibration of aerosol fluorescence spectra and fluorescence correction of humidity
552   measurements, Atmos. Meas. Tech., 16, 1–13, 2023. https://doi.org/10.5194/amt-16-1-2023.

553   Sugimoto, N., Huang, Z., Nishizawa, T., Matsui, I., Tatarov, B.: Fluorescence from atmospheric
554   aerosols observed with a multichannel lidar spectrometer," Opt. Expr. 20, 20800-20807,
555   https://doi.org/10.1364/OE.20.020800, 2012.

556   Veselovskii, I., Hu, Q., Goloub, P., Podvin, T., Korenskiy, M., Pujol, O., Dubovik, O., Lopatin,
557   A.: Combined use of Mie-Raman and fluorescence lidar observations for improving aerosol
558   characterization: feasibility experiment, Atm. Meas. Tech., 13, 6691–6701, 2020.
559   doi.org/10.5194/amt-13-6691-2020.

560   Veselovskii, I., Hu, Q., Goloub, P., Podvin, T., Barchunov, B., and Korenskii, M.: Combining
561   Mie–Raman and fluorescence observations: a step forward in aerosol classification with lidar
562   technology, Atmos. Meas. Tech., 15, 4881–4900, 2022b. https://doi.org/10.5194/amt-15-
563   4881-2022.

564   Veselovskii, I., Kasianik, N., Korenskii, M., Hu, Q., Goloub, P., Podvin, T., and Liu, D.:
565   Multiwavelength fluorescence lidar observations of smoke plumes, Atmos. Meas. Tech., 16,
566   2055–2065, 2023. https://doi.org/10.5194/amt-16-2055-2023

567   Wang, Y., Huang, Z., Zhou, T., Bi, J., Shi J.: Identification of fluorescent aerosol observed by a
568   spectroscopic   lidar   over   northwest   China,   Optics   Express,   31,   22157,
569   https://doi.org/10.1364/OE.493557, 2023.

570   Whiteman, D. N.: Examination of the traditional Raman lidar technique. I. Evaluating the
571   temperature   dependent   lidar   equations,   Appl.   Optics,   42,   2571–2592,
572   https://doi.org/10.1364/AO.42.002571, 2003.

573

Atmospheric
Measurement
Techniques
Open Access
Discussions
EGU

574

Fig.1. Optical layout of depolarization measurements at 408 nm and 466 nm wavelengths. L –
lens; IF1 - IF3 – interference filters, DM1, DM2 – dichroic mirrors, PBS – polarizing cube.

577

578
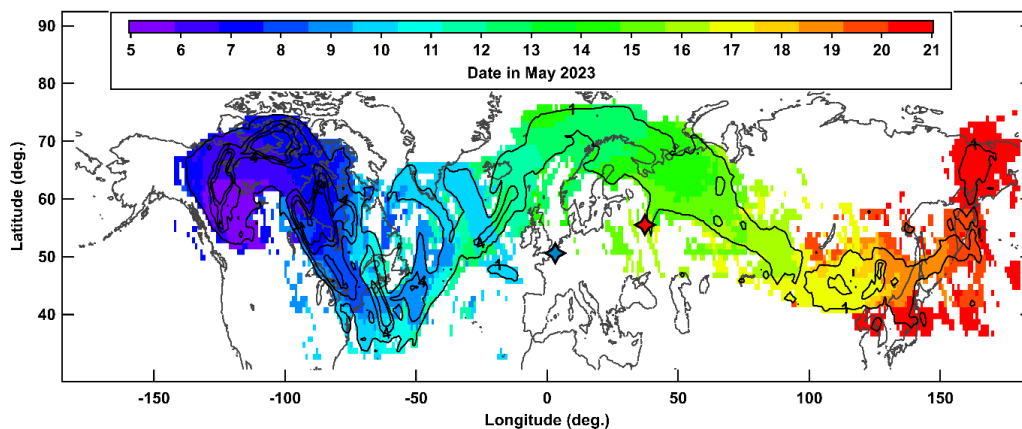
Fig.2. Spatiotemporal evolution of the smoke plume from the wildfire event in Alberta, Canada on

5 May 2023. Color-filled time-coded areas indicate the occurrences of Aerosol Index (AI) values

from OMPS-NPP instrument exceeding 0.5. The actual AI values (1-10) are shown in contours.

The blue and red-filled starts indicate the location of Lille and Moscow lidar stations respectively.

583

584
585
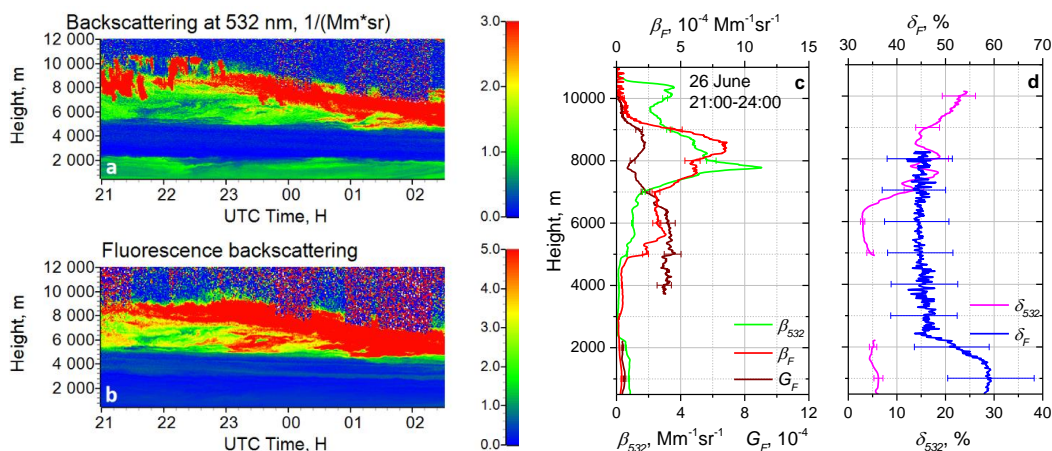
586
587 Fig.3. Smoke event on the night 26-27 June 2023. Spatio-temporal distributions of (a) aerosol
588 backscattering coefficient β_{532} and (b) fluorescence backscattering β_F (in 10^{-4} $Mm^{-1}sr^{-1}$). Vertical
589 profiles of (c) the aerosol β_{532} and fluorescence β_F backscattering coefficients, the fluorescence
590 capacity G_F; (d) the particle δ_{532} and the fluorescence δ_F depolarization ratios.

591
592
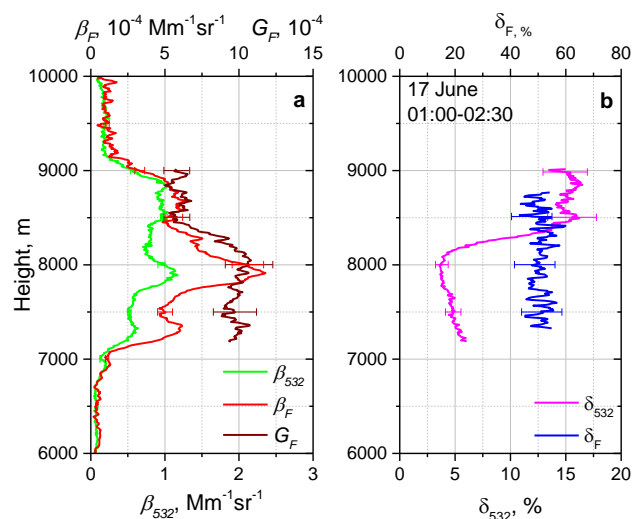
593
594 Fig.4. Vertical profiles of (a) aerosol β_{532} and fluorescence β_F backscattering coefficients,
595 fluorescence capacity G_F and (b) particle δ_{532} and fluorescence δ_F depolarization ratios on the night
596 16-17 June 2023 for period 01:00-02:30 UTC.

597
598

22

599
600
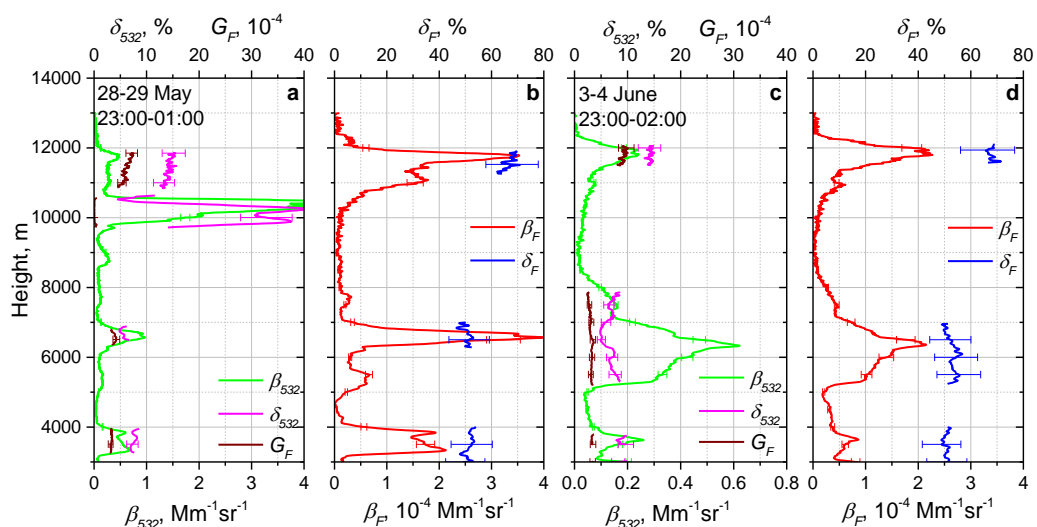
601
602 Fig.5. Vertical profiles of (a, c) backscattering coefficient β_{532}, particle depolarization ratio δ_{532},
603 fluorescence capacity G_F and (b, d) fluorescence backscattering β_F and fluorescence depolarization
604 ratio δ_F for two smoke episodes on the nights 28-29 May 2023 and 3-4 June 2023.
605
606

Atmospheric
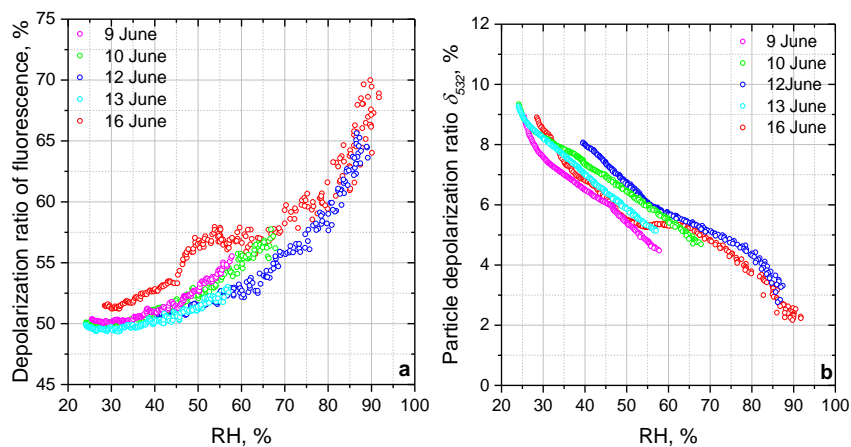Measurement
Techniques
Discussions

Open Access

EGU

607

608
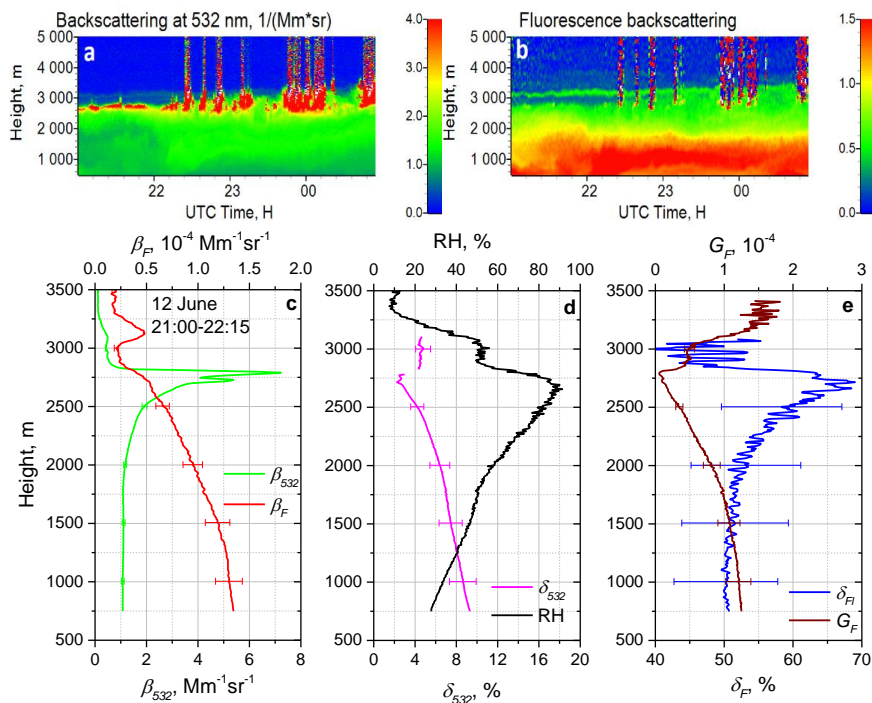
609
610 Fig.6. Particle hygroscopic growth in the boundary layer on the night 12-13 June 2023. Spatio-
611 temporal distributions of (a) aerosol backscattering coefficient β_{532} and (b) fluorescence
612 backscattering β_F (in 10^{-4} $Mm^{-1}sr^{-1}$). Vertical profiles of (c) aerosol β_{532} and fluorescence β_F
613 backscattering coefficients; (d) particle depolarization ratio δ_{532} and the relative humidity RH; (e)
614 fluorescence depolarization ratio δ_F and fluorescence capacity G_F for the time period 21:00-22:15
615 UTC.
616

Atmospheric
Measurement
Techniques
Discussions

617
618
619

620
621 Fig.7. (a) Fluorescence depolarization ratio and (b) particle depolarization ratio δ_{532} as a function
622 of the relative humidity in the boundary layer for the measurements on 9, 10, 12, 13, 16 June 2023.
623
624
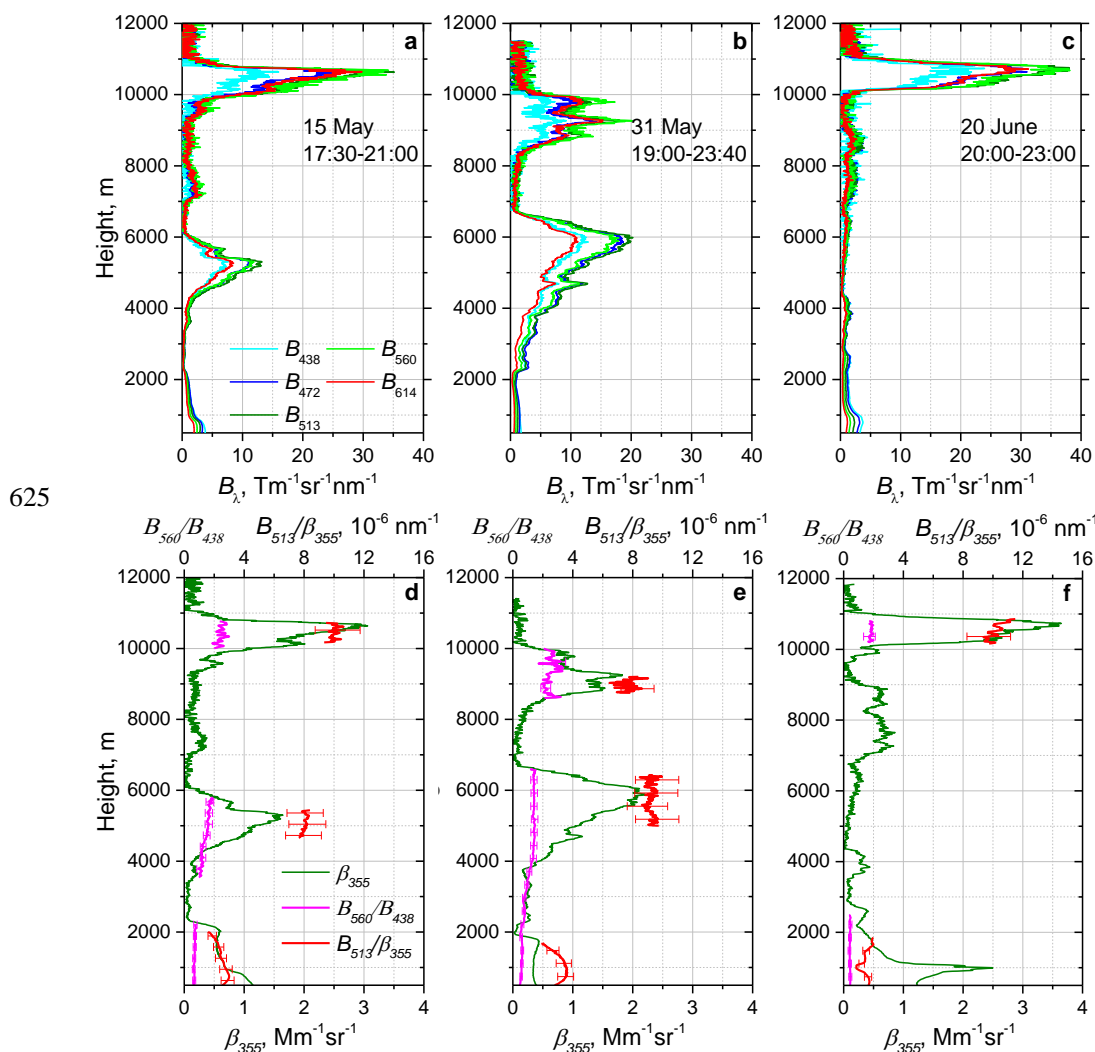
Fig. 8. Fluorescence measurements in Moscow on 15 May, 31 May, 20 June 2023. Vertical profiles of (a-c) fluorescence spectral backscattering coefficients B_λ at 438, 472, 513, 560, 614 nm and (d-f) aerosol backscattering coefficient β_{355}, the ratio B_{560}/B_{438} and B_{513}/β_{355}. Measurements were performed at an angle of 48 dg to horizon.
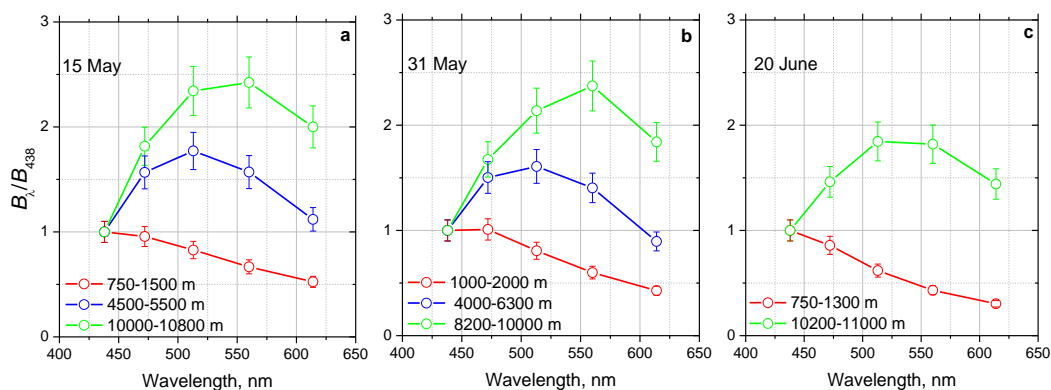
Fig.9. Fluorescence spectra B_λ/B_{438} at different height intervals measured during smoke episodes on 15 May, 31 May, 20 June 2023 for the same temporal intervals as in Fig.8.

636
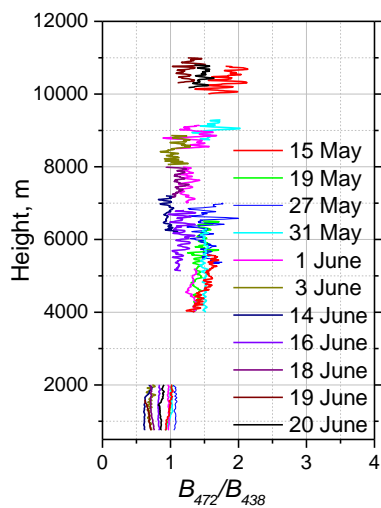
Fig.10. Height profiles of ratio B_{472}/B_{438} for smoke episodes during 15 May – 20 June 2023. Smoke
layers start above 4000 m.

639
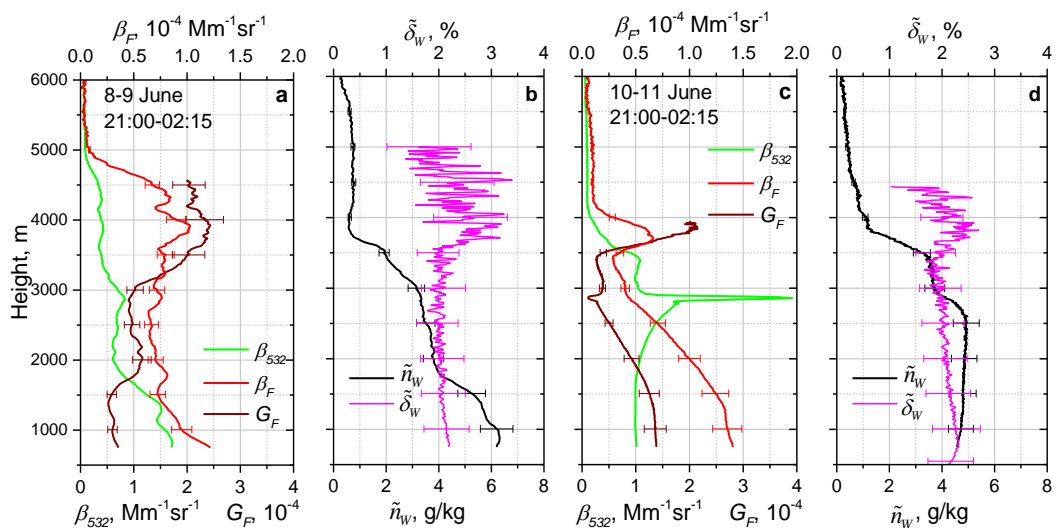
Fig.11. Impact of aerosol fluorescence on the depolarization ratio in the water vapor Raman channel on the nights 8-9 and 10-11 June 2023 at Lille. Vertical profiles of (a, c) particle backscattering β_{532}, fluorescence backscattering β_F, fluorescence capacity G_F and (b, d) depolarization ratio $\tilde{\delta}_W$ of water vapor Raman signal and the water vapor mixing ratio $\tilde{n}_W$.
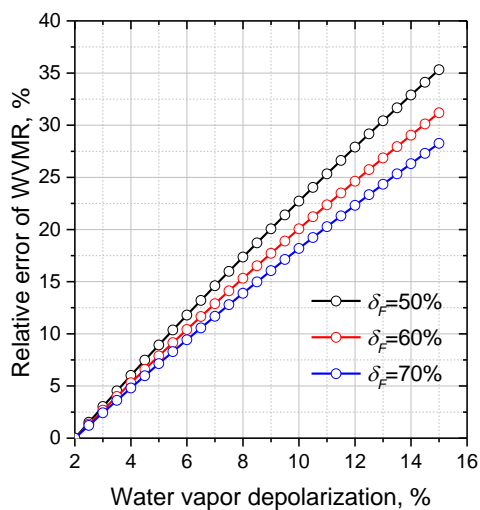
Fig.12. Relative error of water vapor mixing ratio (WVMR) $\frac{\Delta n_W}{\tilde{n}_W}$ induced by the fluorescence a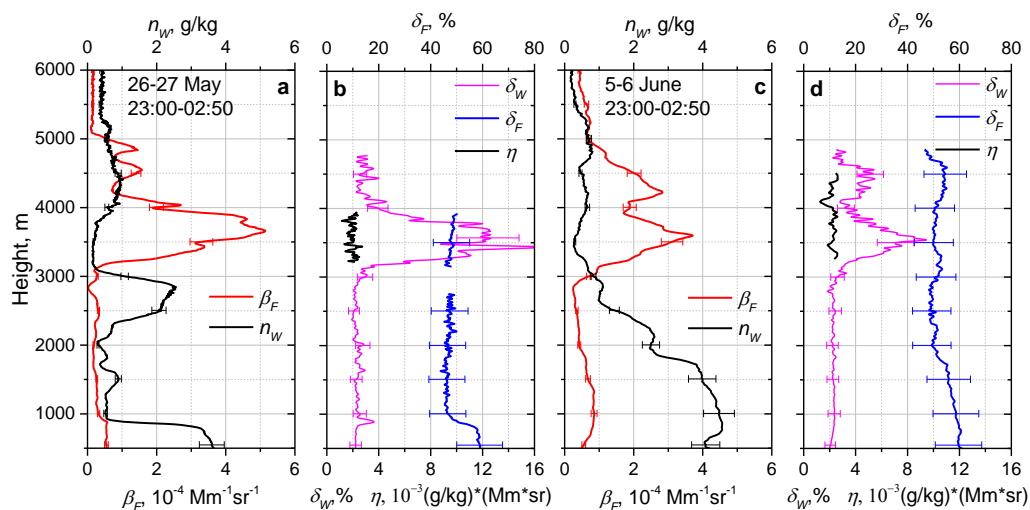s a function of depolarization ratio $\tilde{\delta}_W$ in the water vapor Raman channel for three values of fluorescence depolarization ratio $\delta_F=50\%$, 60%, 70%. The depolarization ratio of water vapor Raman backscatter in the absence of fluorescence is assumed to be $\delta_W=2\%$.

Atmospheric
Measurement
Techniques
Discussions

Open Access

EGU

653
654

655

656 Fig. 13. Fluorescence measurements in Lille on the night 26-27 May and 5-6 June 2023. (a, c)
657 Vertical profiles of the fluorescence backscattering β_F, the water vapor mixing ratio $\tilde{n}_W$, (b, d) the
658 depolarization ratio of water vapor Raman signal $\tilde{\delta}_W$, the fluorescence depolarization ratio δ_F and
659 parameter η, describing contribution of fluorescence to the water vapor channel.
660

661

662
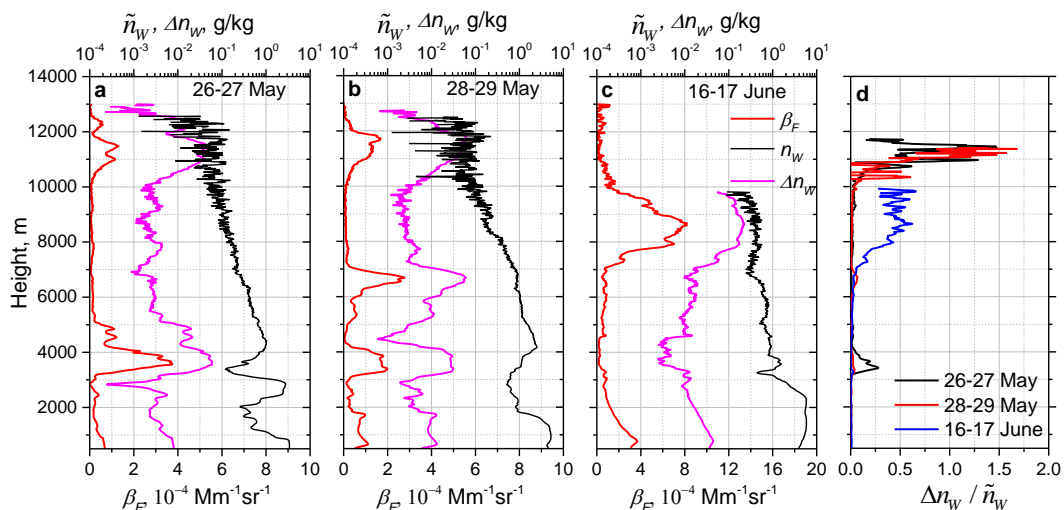
663
664 Fig.14. Impact of smoke fluorescence on the water vapor measurements. Vertical profiles of
665 fluorescence backscattering β_F, water vapor mixing ratio $\tilde{n}_W$ and bias in water vapor channel Δn_W
666 provided by the fluorescence of smoke for episodes on the nights (a) 26-27 May, (b) 28-29 May
667 and (c) 16-17 June 2023 for time interval 21:00-02:30 UTC. (d) Error $\dfrac{\Delta n_W}{\tilde{n}_W}$ introduced by smoke
668 fluorescence for three episodes.
669